The Astrophysical Journal, 981:76 (13pp), 2025 March 1
https://doi.org/10.3847/1538-4357/ada93c

Simulating the Arrival of Multiple Coronal Mass Ejections That Triggered the Gannon Superstorm on 2024 May 10

Smitha V. Thampi[1], Ankush Bhaskar[1], Prateek Mayank[2], Bhargav Vaidya[2], and Indu Venugopal[1,3]
[1] Space Physics Laboratory, Vikram Sarabhai Space Centre, Thiruvananthapuram, 695022, India
[2] Department of Astronomy, Astrophysics and Space Engineering, Indian Institute of Technology-Indore, Madhya Pradesh, 453552, India
[3] Department of Physics, CUSAT, Kochi, 682022, India

Received 2024 November 11; revised 2025 January 9; accepted 2025 January 10; published 2025 February 27

Abstract

The 2024 May 10 space weather event stands out as the most powerful storm recorded during the current solar cycle. This study employs a numerical framework utilizing a semiempirical coronal model, along with heliospheric upwind extrapolation with time dependence and cone coronal mass ejection (CME) models for the inner heliosphere, to forecast solar wind velocity and the arrival of CMEs associated with this event. The simulations were also carried out using the Space Weather Adaptive Simulation framework and a drag-based model (DBM) for this complex event of multiple CMEs. Predicted arrival times and velocities from these models are compared with actual observations at the Sun–Earth L1 point. These simulations reveal that three CMEs reached Earth nearly simultaneously, resulting in the extreme space weather event, followed by the arrival of a few more eruptions. The simulations accurately predicted arrival times with a discrepancy of approximately 5 hr or less for these CMEs. Further, the ensemble study of the DBM shows the sensitivity of the CME arrival time to the background solar wind speed and drag parameters. All three models have done fairly well in reproducing the arrival time closely to the actual observation of the CMEs responsible for the extreme geomagnetic storm of 2024 May 10. These rare solar storms offered a unique opportunity to thoroughly evaluate and validate our advanced models for predicting their arrival at Earth.

Unified Astronomy Thesaurus concepts: Heliosphere (711); Solar-terrestrial interactions (1473); Space weather (2037); Solar coronal mass ejections (310); Solar wind (1534)

1. Introduction

Extreme space weather events, driven by intense solar activity, can be initiated by powerful coronal mass ejections (CMEs) at the Sun. The arrival of these transients from the Sun causes geomagnetic storms in Earth's near-space environment, which have the potential to severely disrupt our technological systems. A notable historical example is the Carrington event of 1859, which caused widespread telegraph failures and auroras at unusually low latitudes (B. T. Tsurutani et al. 2003; G. Siscoe et al. 2006; H. Hayakawa et al. 2022). Another case are the Halloween storms that occurred during solar cycle (SC) 23. These were a series of intense solar storms between late October and early November in 2003, driven by a series of CMEs. The Halloween storms caused widespread disruptions, including satellite anomalies, GPS navigation issues, and power system disturbances across various regions, exposing the vulnerability of modern technological infrastructure to such extreme space weather events. The intense storms also caused auroras to be visible at much lower latitudes than usual.

In the current solar cycle (SC 25), a powerful solar storm impacted Earth in early 2024 May. This event was triggered by the intense activity from NOAA Active Region 13664 of the Sun. This region unleashed a series of X-class flares and CMEs during 2024 May 8–9 that were directed toward Earth. The resulting geomagnetic storm was very intense, reaching extreme (NOAA G5) levels (Minimum Dst index ~ -412 nT). This is the biggest geomagnetic storm since 2003 in terms of its strength, and the active region on the Sun was as big as the Carrington event (B. T. Tsurutani et al. 2003; H. Hayakawa et al. 2019). This series of events is now being called the "Gannon Superstorm of 2024," in honor of the space weather physicist Jenn Gannon (Y. Yamazaki et al. 2024). Such extreme events underscore the importance of space weather forecasting, not only to the research community but also to governments, the space sector, and industry stakeholders (C. J. Schrijver et al. 2015).

The models that predict the arrival of these events generally use solar photospheric magnetic field observations as their basic input and use either empirical or semiempirical methods, or magnetohydrodynamics (MHD)–based simulations to arrive at solar wind parameters at different points in the heliosphere. In one of the earliest studies, N. Lugaz et al. (2005) performed a three-dimensional compressible MHD model simulating the interaction between two CMEs and showed the complexity of magnetic interactions and a steep acceleration of the shock. Almost all models use a coupled two-domain procedure to arrive at solar wind parameters near Earth and other planets. In this study, we use the Wang-Sheeley-Arge (WSA) approach in the coronal domain and the heliospheric upwind extrapolation with time dependence (HUXt; M. Owens et al. 2020; L. Barnard & M. Owens 2022) with the cone CME model in the inner heliospheric domain, to arrive at the temporal variation of solar wind velocity for the period 2024 May 9–15. The predicted arrival times and velocities are compared with the ensemble drag-based model (DBM), as well as actual observations at the Sun–Earth L1 point.

2. Model Details

2.1. HUXt-based Solar Transient Arrival Framework

This numerical framework for predicting the solar wind velocity and arrival of CMEs is based on established schemes that use a semiempirical coronal model along with the HUXt

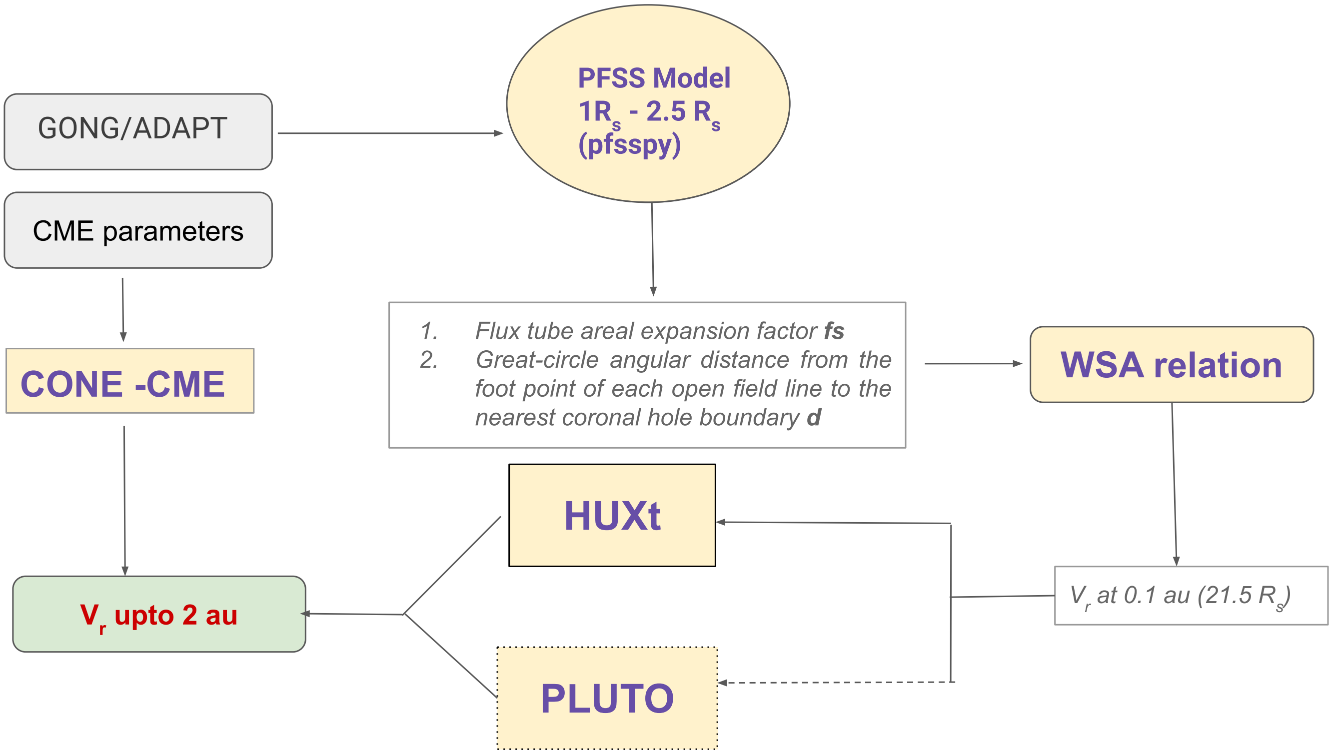

Figure 1. The flowchart depicting the details of the STAR and SWASTi MHD models. The STAR model is based on the PFSS coronal model, WSA semiempirical relation, and HUXt with cone CME, whereas the SWASTi model is based on the PFSS coronal model, WSA semiempirical relation, and PLUTO-MHD code with cone CME.

(M. Owens et al. 2020; L. Barnard & M. Owens 2022; M. Owens & L. Barnard 2024a) and cone CME models for the inner heliosphere. Figure 1 summarizes the details of the Solar Transient Arrival (STAR) module. Unlike MHD models, this module is capable of simulating the solar wind velocity alone and not other properties like density, magnetic field, and temperature. However, this approach is computationally simple and inexpensive to analyze the arrival of transient events, since it is based on the HUXt code. The basic input to the coronal domain are the synoptic maps of magnetograms, provided by the Global Oscillation Network Group (GONG) or Helioseismic Magnetic Imager (HMI) maps. The potential field source surface (PFSS) model solves the Laplace equation from the solar surface to a source surface (at 2.5R_s, where R_s is the solar radius) from where the field is assumed to be radial. We have used the PFSSPY package (D. Stansby et al. 2020, 2023) for this calculation, which is solved on a rectilinear grid that is equally spaced in ln(r), cosθ, and ϕ in spherical coordinates. A grid resolution of 100 × 181 × 361 is used to solve for field lines from the solar surface to the source surface, which is at a radius of 2.5R_s in our case. The field lines are then traced to get the regions of closed and open field lines and the coronal hole boundaries. The expansion factor of open field lines (f) is then obtained by

$$f = \frac{R_s}{R_{ss}} \frac{B_r(R_s, \theta, \phi)}{B_r(R_{ss}, \theta, \phi)}. \qquad (1)$$

This equation is the same as that given in previous works (e.g., (J. Pomoell & S. Poedts 2018; P. Mayank et al. 2022), which defines the flux tube expansion factor using only the radial magnetic field component. In addition to this factor, the great circle angular distance d from the footpoint of each open field line to the nearest coronal hole boundary is also computed. These two factors are used in the following empirical relation for solar wind velocities characterizing the ambient solar wind at 21.5R_s for a given flux tube. We have adopted the following equation:

$$v(f, d) = v_0 + \frac{v_1}{(1+f)^{\alpha}} \times [(1 - 0.8\exp(-d/w)^{\beta}))^3], \qquad (2)$$

where $v_0 = 250\,\mathrm{km\,s^{-1}}$, $v_1 = 650\,\mathrm{km\,s^{-1}}$, $\alpha = 2/9$, $w =$ median of d, and $\beta = 1.25$.

It may be noted that several different forms for calculating the solar wind speed as a function of f and d are available in the literature (e.g., C. N. Arge & V. J. Pizzo 2000; P. Riley et al. 2001; S. L. McGregor et al. 2011; J. Pomoell & S. Poedts 2018; P. Mayank et al. 2022).

The equation we used is the same as that used by P. Mayank et al. (2022) for their MHD model, in which w is taken as the median of d. In several other works, w is taken as a constant value, e.g., w is 0.02 rad in J. Pomoell & S. Poedts (2018). However, a difference from P. Mayank et al. (2022) is that they have used $v_0 = 240\,\mathrm{km\,s^{-1}}$, $v_1 = 725\,\mathrm{km\,s^{-1}}$ for their HUX (not the time-dependent version) run, but we have found that for HUXt $v_0 = 250\,\mathrm{km\,s^{-1}}$, $v_1 = 650\,\mathrm{km\,s^{-1}}$ is appropriate.

Equation (2) provides the inner boundary conditions to HUXt, which is based on incompressible hydrodynamics, which takes a reduced-physics approach to calculate only the solar wind velocity, employing approximations to greatly reduce the complexity of the MHD momentum equation. In this computation, the solar wind is assumed to be purely radial and is modeled by Burger's equation (L. Barnard & M. Owens 2022). Since HUXt maintains explicit time dependence, structures such as CMEs can be incorporated (L. Barnard &

Table 1
Summary of the Input CME Parameters Used for Different Simulations, in the Heliocentric Earth Equatorial Frame

CME ID	CME Initiation Time	Time at $21.5R_s$	CME Speed ($\mathrm{km\ s^{-1}}$)	Longitude (deg)	Latitude (deg)	Half-angle (deg)
CME-1	2024-05-08T05:36	2024-05-08T09:30	870.0	9.0	−7.0	43.0
CME-2	2024-05-08T12:24	2024-05-08T16:58	776.0	3.0	−5.0	45.0
CME-3	2024-05-08T19:12	2024-05-08T23:27	828.0	−23.0	3.0	38.0
CME-4	2024-05-09T18:23	2024-05-09T20:27	1236.0	12.0	−5.0	45.0
CME-5	2024-05-10T07:12	2024-05-10T10:35	1018.0	31.0	−2.0	41.0
CME-6	2024-05-11T01:36	2024-05-11T04:22	1263.0	51.0	0.0	51.0

M. Owens 2022). To do this, the STAR code employs the cone CME model (D. Odstrcil & V. J. Pizzo 1999), which treats the CMEs as hydrodynamic clouds and is introduced as a time-dependent boundary condition at the inner radial boundary at $21.5R_s$. The cone model parameters are obtained from the CCMC Space Weather Database Of Notifications, Knowledge, Information (DONKI) database.

The PFSSPY (D. Stansby et al. 2020, 2023) code is obtained from https://pfsspy.readthedocs.io/en/latest/installing.html. The HUXt code is downloaded from Zenodo (M. Owens & L. Barnard 2024a, 2024b) and utilized for further analysis.

2.2. Space Weather Adaptive Simulation Framework (SWASTi)

We have also used the Space Weather Adaptive Simulation framework (SWASTi; P. Mayank et al. 2022, 2023) to study this highly geo-effective event. SWASTi is a physics-based modular framework that solves the MHD equations to simulate the solar wind and CMEs in the inner heliosphere. In this study, the MHD domain extends radially from 0.1 to 2.1 au. The simulation employs a synoptic magnetogram as the observational input for the solar wind model, with the initial solar wind speed (V_r) at 0.1 au determined using a modified WSA speed relation (see Equation (2)) and other initial properties calculated using the following empirical relations based on fast solar wind characteristics:

$$n = n_0 \left(\frac{V_{f\mathrm{sw}}}{V_r}\right)^2 \tag{3}$$

$$B_r = \mathrm{sgn}(B_{\mathrm{corona}})\, B_0 \left(\frac{V_r}{V_{f\mathrm{sw}}}\right) \tag{4}$$

$$B_\phi = -\, B_r \sin\theta \left(\frac{V_{\mathrm{rot}}}{V_r}\right), \tag{5}$$

where n is the plasma number density, B_r and B_ϕ are the radial and azimuthal components of the magnetic field, sgn(B_{corona}) is the polarity of the extrapolated coronal magnetic field, and V_{rot} is the rotational speed of the inner boundary corresponding to the time span of the magnetogram. Here n_0 and B_0 refer respectively to the number density and magnetic field values of the fast solar wind with speed $V_{f\mathrm{sw}}$. In this work, the default values of these parameters are taken, which are $n_0 = 200\ \mathrm{cm}^{-3}$, $B_0 = 300$ nT, and $V_{f\mathrm{sw}} = 650\ \mathrm{km\ s}^{-1}$. The initial thermal pressure (at 0.1 au) is kept constant at 6.0 nPa, and the meridional and azimuthal components of velocity (V_θ and V_ϕ) are assumed to be zero initially.

Within the SWASTi framework, there are two distinct CME models: the elliptic cone and flux rope CME models. The cone model features a simple nonmagnetic geometry, whereas the flux rope model incorporates a complex 3D magnetic field configuration (P. Mayank et al. 2023). To ensure consistency between the MHD simulation and the results of STAR and DBM-based CMEs in this work, we used the cone model with the same initial properties described in Table 1. The half-width and half-height of the CME are set equal to the half-angle. Additionally, the CME properties at $21.5R_s$, including arrival time and speed, as well as the eruption coordinates on the solar surface, are consistent with those listed in Table 1. For simplicity, we have assumed a constant temperature of 0.8 MK and a density of $2 \times 10^{-18}\ \mathrm{kg\ m}^3$ for all CMEs.

2.3. Drag-based Model for CME Propagation and Arrival Time

The DBM relies on MHD drag, which is caused by the emission of MHD waves in the collisionless solar wind, rather than kinetic drag in a fluid (P. J. Cargill et al. 1996). This drag modulates the speed of CMEs to that of the surrounding solar wind. In interplanetary space, CMEs are influenced by the Lorentz force (F_{L}), gravity (F_G), and MHD aerodynamic drag (F_D). Thus, the net force acting on the CME can be expressed as

$$F = F_{\mathrm{L}} + F_G + F_D. \tag{6}$$

The analytical DBM is a commonly used model for the heliospheric propagation of CMEs and is valued for its simplicity and quick calculations. The DBM considers CME propagation as a momentum exchange with the ambient solar wind. However, the DBM is mainly driven by MHD drag, which aligns the CME speed with the ambient solar wind.

The following equation from P. J. Cargill (2004) represents the propagation of the CMEs or shock in the background solar wind:

$$\begin{aligned} a(t) = \frac{dV_{\mathrm{CME}}}{dt} &= \frac{F_D}{\mathrm{M}_*} \\ &= -\gamma \mathrm{C}_D (V_{\mathrm{CME}}(t) - V_{\mathrm{SW}}) |V_{\mathrm{CME}}(t) - V_{\mathrm{SW}}|, \end{aligned} \tag{7}$$

where $a(t) = \frac{d^2R(t)}{dt^2}$ represents the CME acceleration, $M_* = M_{\mathrm{CME}} + M_v$, where M_{CME} is the mass of the interplanetary coronal mass ejection (ICME) and M_v is the "virtual mass," defined approximately as $M_v = \rho_{\mathrm{sw}}\tau/2$, where τ is the volume of the ICME. Parameter ρ_{sw} is the solar wind density. $V_{\mathrm{CME}}(t)$ represents the CME speed; $R(t)$ represents the heliospheric distance; $\gamma = \frac{\rho_{\mathrm{SW}} A}{\tau(\rho_{\mathrm{CME}} + \rho_{\mathrm{SW}}/2)}$ represents the drag parameter, which describes the rate of change of CME speed and is assumed to be constant; and V_{SW} represents the solar wind speed, also assumed to be constant. The quantity $(\gamma C_D)^{-1}$ represents a characteristic deceleration length. Further, the advanced DBM (ADBM) accounts for the shape of CMEs and solves the equation of motion for the CME geometry. The geometry could be approximated by a flat front, or a semicircular or circular shape (R. Schwenn et al. 2005). The propagation of CME can be determined by analyzing the evolution of two types of 2D cone geometry: (a) self-similar cone evolution, and (b) flattening cone evolution (M. Dumbović et al. 2021). The DBM has been compared with other existing models of CME propagation and found to be doing fairly well (B. Vršnak et al. 2014). The DBM takes the following inputs: CME speed (V_{CME}) at certain distance, half-width of CME (θ_{CME}), and propagation direction (longitude, ϕ_{CME}); the solar wind radial speed (V_{SW}); the drag parameter (γ); and the target direction (longitude, ϕ_T). The codes of the advanced DBM (ADBM) model open-source codes available on Zenodo are adapted for the study (R. Mugatwala & B. Vaidya 2021). The determination of initial parameters like background solar wind speed (V_{sw}) and drag parameter (γ) is always the open issue (M. Dumbović et al. 2021). Various approaches have been adopted based on physics-based/empirical models and in situ observations. It has been observed that $V_{\mathrm{sw}} = 450\,\mathrm{km\,s^{-1}}$ and $\gamma = 0.2 \times 10^{-7}$ are optimum parameters (B. Vršnak et al. 2012, 2014), which generally work for high or low solar activity. Here we used these values as mean values and assumed their Gaussian distribution to study their impact on CME arrival time and velocity at Earth.

As mentioned, the DBM models CME propagation as a momentum exchange between the CME and the ambient solar wind, assuming an ambient solar wind density that falls off as $\frac{1}{r^2}$. This results in the ICME cross section increasing as $A \propto r^2$ with constant mass and γ. However, other studies show that the CME cross section increases as $A \propto r^{1.6}$, which is slower than the DBM assumption (V. Bothmer & R. Schwenn 1997). The DBM assumes isotropic, constant-speed solar wind, oversimplifying since ICME propagation can alter the solar wind structure. It also ignores CME–CME interactions, where a fast CME can accelerate a slower one launched earlier. However, this is computationally very fast and provides realistic predictions. The model has been compared with the WSA-ENLIL+CONE model and found to be reasonably comparable in the prediction of CME arrival time (B. Vršnak et al. 2014).

3. Data

As mentioned, the STAR module is capable of generating the inner boundary conditions for HUXt, by using GONG-synoptic, GONG Air Force Data Assimilative Photospheric Flux Transport (GONG-ADAPT; K. S. Hickmann et al. 2015), and HMI maps. For the present study, we used both GONG-synoptic and GONG-ADAPT as inputs for solving the PFSS coronal model. For providing the synoptic magnetograms required by the PFSS model, both the hourly updated standard synoptic magnetogram (GONG-synoptic) maps and the ADAPT maps are used. For this study, the hourly updated integral Carrington rotation (CR) synoptic maps are downloaded from https://gong.nso.edu/data/magmap/QR/bqj, for CR2284. We have used the GONG maps generated on 2024 May 9 and 10 in different simulations. These maps contain information of the photospheric magnetic field corresponding to the period from 2024 April 17 15:28 UTC to 2024-05-14 21:12 UTC. The six two-hourly ADAPT maps obtained on 2024 May 10 (00:00-10:00 UTC), downloaded from https://gong.nso.edu/adapt/maps/gong/2024, are also used for simulations.

The CME parameters are taken from the DONKI website.[4] For the given time period, the DONKI database lists many CMEs, of which some are slow (less than $500\,\mathrm{km\,s^{-1}}$) or narrow (half-width less than 35°) or not directed toward Earth (source longitude not within ±60° heliocentric Earth equatorial) and are excluded, and the remaining six CMEs that erupted on 2024 May 8–9 are selected for modeling. The selected CMEs originated from NOAA AR 13664 of the Sun. The parameters of the six selected CMEs are provided in Table 1. In these, CME-1–CME-5 are used in all STAR, DBM, and SWASTi simulations, whereas CME-6 is only used in certain cases, as explained later. The interplanetary magnetic field (IMF), solar wind speed, density, and dynamic pressure measurements near the Sun–Earth L1 point and the SYM-H (representing the ring current) variation at Earth are obtained from the NASA Space Physics Data Facility (SPDF) OMNIWeb data center, with 5-minute temporal resolution.[5] The actual CME shock arrival times are taken from https://kauai.ccmc.gsfc.nasa.gov/CMEscoreboard/. Additionally, the CME arrival time corresponding to MHD simulation using the SWASTi framework is also presented in this study. For the MHD simulations, we have used the GONG-ADAPT magnetogram.

4. Results

Figure 2 shows the solar wind parameters and the geomagnetic SYM-H index for the period 2024 May 8–14. The parameters shown here are solar wind velocity (V), density (Den.), dynamic pressure (Dyn. P), temperature (T), total IMF and its components, and the geomagnetic SYM-H index in panels (a)–(e), respectively. It can be seen that the arrival of the first shock is clearly seen around 16:45 UTC on 2014 May 10, with an enhancement in solar wind speed, density, and magnetic field. A possible flux rope signature can be observed around ∼21:30 UTC, which corresponds to a second, more intense amplification of magnetic field components, with $|B|$ reaching a maximum of ∼75 nT. For this flux rope feature, which extends to 09:30 on May 11, there are three noticeable decreases in density, which may correspond to three CMEs that may have merged into the signature. The southward B_z component became almost −50 nT in the early hours of 2024 May 11. The enhanced solar wind density and speed (750–$950\,\mathrm{km\,s^{-1}}$) prevailed between May 11 and 12. The maximum SYM-H value of ∼ −412 nT was observed around 03:00 UTC on May 11. Though the major geomagnetic field enhancements lasted only up to May 12, the velocity continued to remain high on May 13 as well, with another enhancement of density with lesser magnitude compared to the previous days.

Figure 3 shows the results of the STAR simulations for 2024 May 9–15, with GONG maps as input, along with the solar wind speed observations at L1. Figure 3(a) shows the simulation done with the GONG map obtained on 2024 May 9 at 23:14 UTC. The output of the simulation is shifted backward by 3.5 hr to match with

---

[4] https://kauai.ccmc.gsfc.nasa.gov/DONKI/search/

[5] https://omniweb.gsfc.nasa.gov/

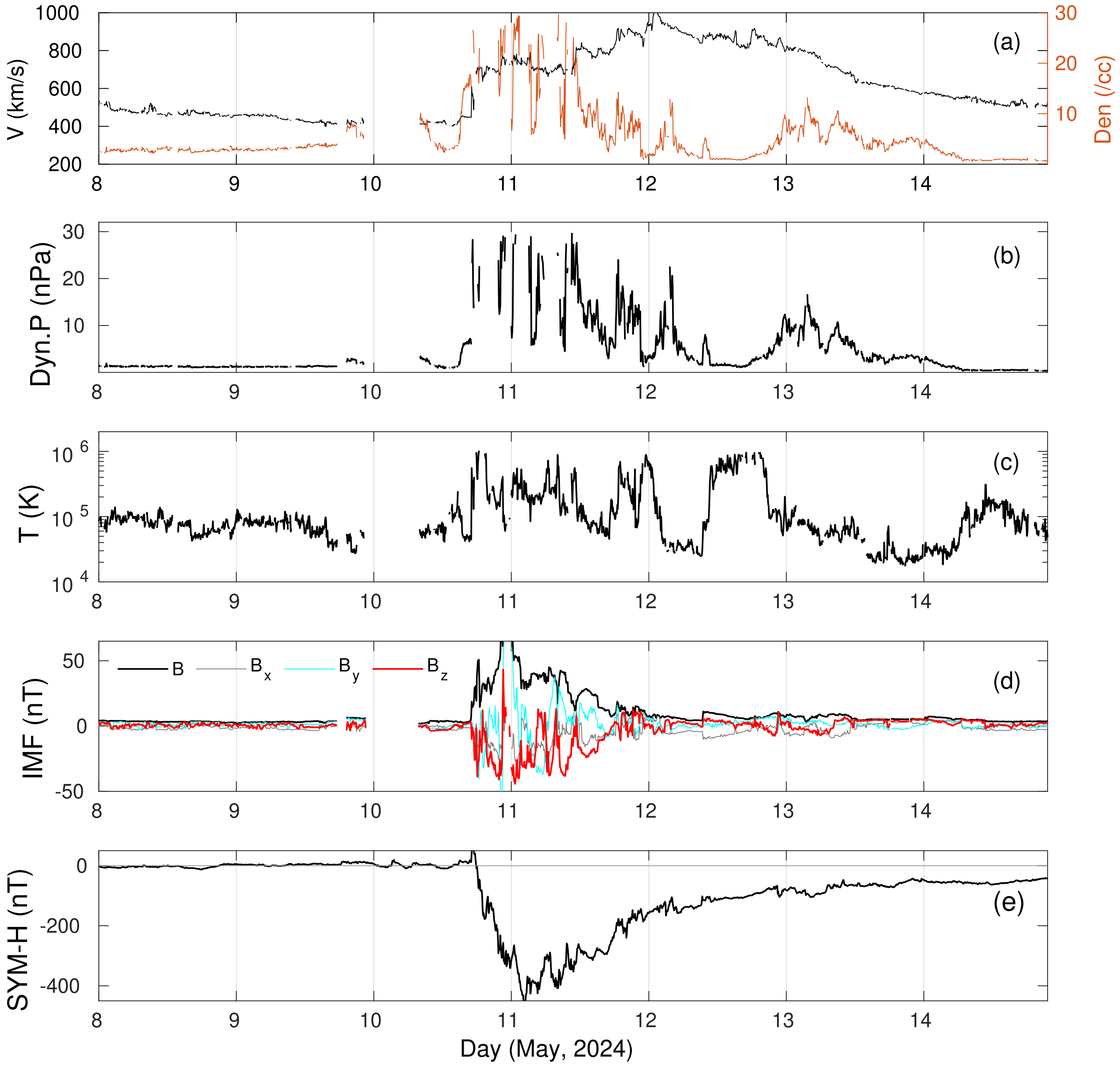

Figure 2. The temporal variations of (a) solar wind speed (left y-axis) and solar wind density (right-y-axis), (b) solar wind dynamic pressure, (c) temperature, (d) IMF measured at Sun–Earth L1, and (e) the SYM-H variation at Earth for the period 2024 May 8–14.

the first CME arrival as shown in the figure. The motivation behind applying the time shift to the simulations is to compare the observed and simulated CME-related enhancements in speeds and their temporal variation in a scenario where we had correctly predicted the arrivals. The time shifting also allows for quantification of the error in CME arrival time for the best-fit result.

Five CMEs are used for this simulation, and it is seen that the first three CMEs arrive nearly simultaneously to generate the first peak in velocity, followed by the subsequent arrivals of the other two CMEs. It can be seen that the solar wind speed of the first merged CME arrival is also higher than that observed at L1. The subsequent peaks are more or less comparable with observations but shifted in terms of structure and arrival times. The overall rms error (RMSE) is 100.6 km s^{-1}, with time-shifted simulation output and observations.

Figure 3(b) shows the STAR simulation done with the GONG map obtained on 2024 May 10 at 08:04 UTC. Here we can see that the magnitude of the initial background velocity and the velocity peaks due to the arrival of the CMEs match better with the observations. However, the time series is shifted by 8 hr to match with the first CME arrival. The lower background velocity in this case might have allowed only a slower propagation for the CMEs in the inner heliosphere domain of the model. The overall RMSE is 112.2 km s^{-1}, with an 8 hr shifted simulation output and observations.

An interesting point to note here is that the simulated solar wind velocity steadily decreased after May 12 and the enhanced solar wind observed on May 13 is not reproduced. Therefore, we have incorporated one more CME (CME-6 in Table 1) into the model, and Figure 3(c) shows the output. This

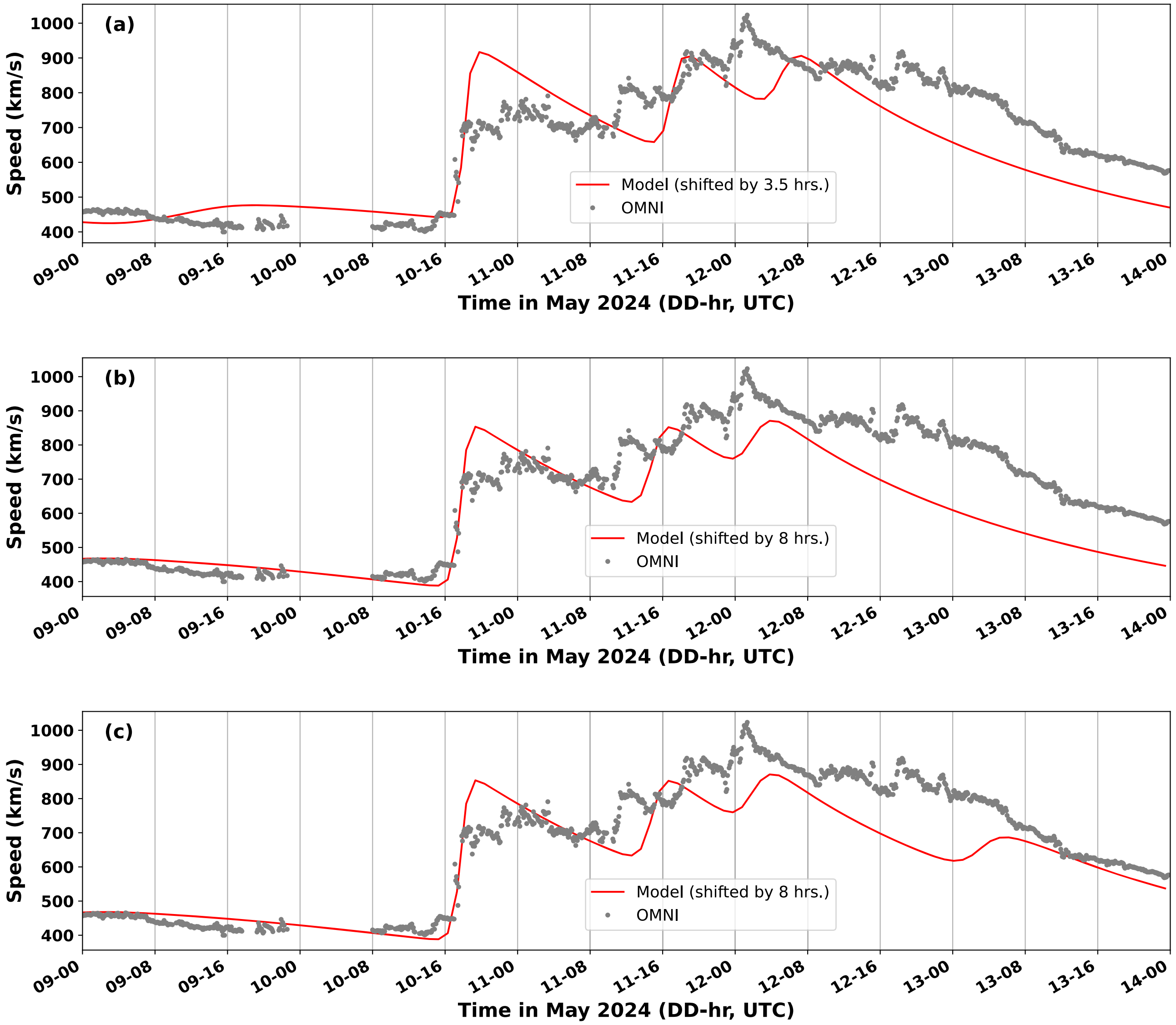

Figure 3. The solar wind velocity simulated by the STAR module (red lines) compared with actual observations (circles). (a) Simulations with the GONG map obtained on May 9. (b, c) Simulations with the GONG map obtained on May 10 with different CME inputs.

has allowed the model to somewhat capture the enhancement in solar wind speed on May 13, and the RSME between time-shifted model output and observations is reduced to 94 km s^{-1}. These simulations convincingly reveal the following aspects: (a) Three CMEs (CME-1, CME-2, and CME-3 in Table 1) arrive at L1 almost simultaneously and cause the first enhancement in the solar wind parameters. CME-3 is the fastest and takes the least time to arrive at Earth. CME-1 takes the longest time to arrive at Earth. (b) Two more, faster CMEs (CME-4 and CME-5 in Table 1) erupted on May 9 and 10 and arrived at Earth subsequently on the next days. (c) The passage of yet another CME (CME-6 in Table 1) is the probable cause of the continued enhancement in solar wind velocity observed on 2024 May 13.

Figure 4 shows the average of the six STAR simulations using the six ADAPT maps obtained on 2024 May 10, at least ~6 hr before the arrival of the event (00 UTC, 02 UTC, 04 UTC, 06 UTC, 08 UTC and 10 UTC), and the six CMEs as inputs to the model. Here the time shift applied to match with the observations is 5 hr, and arrival times for each simulation differ only by minutes. The RMSE for the average of the time-shifted ADAPT simulations and observations is 91.459 km s^{-1}. Figure 5 shows the snapshots of the radial maps from these simulations. Figure 5(a) shows the condition before the CME arrival at L1 and just after the launch of the first CME (on May 8 05:36 UTC at 21.5R_s) into the model. Figure 5(b) shows the snapshot close to the arrival of the three CMEs (merged) at L1. CME-4 and CME-5 (launched on May 9 18:23 UTC and May 10 07:12 UTC, respectively) are also seen in the inner heliosphere. Figure 5(c) shows the snapshot close to the arrival of CME-4, whereas CME-5 is still behind. We can see that CME-1, CME-2, and CME-3 arrived at Earth nearly simultaneously, whereas CME-4 and CME-5 arrived at distinctly different times. Finally, Figure 5(d) shows the glancing arrival of CME-6 on May 13, which could only cause velocity and density enhancements without change in IMF magnitude or direction.

All six CMEs were also simulated using the cone model of the SWASTi framework. Figure 6 shows the results of this simulation. The top two panels illustrate the speed and scaled density profiles in the equatorial plane on 2024 May 12 at UTC 05:16. Four CME shock fronts are visible in these 2D plots.

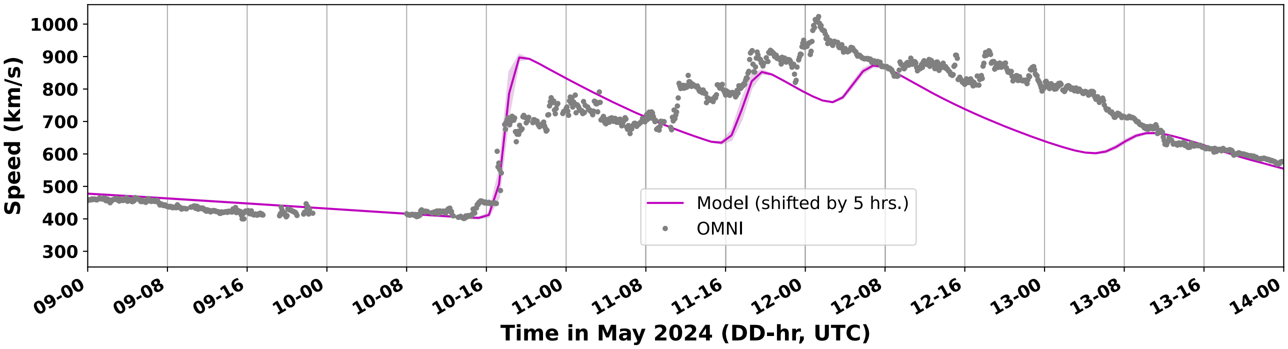

Figure 4. The solar wind velocity simulated by the STAR module using GONG-ADAPT maps compared with actual observations.

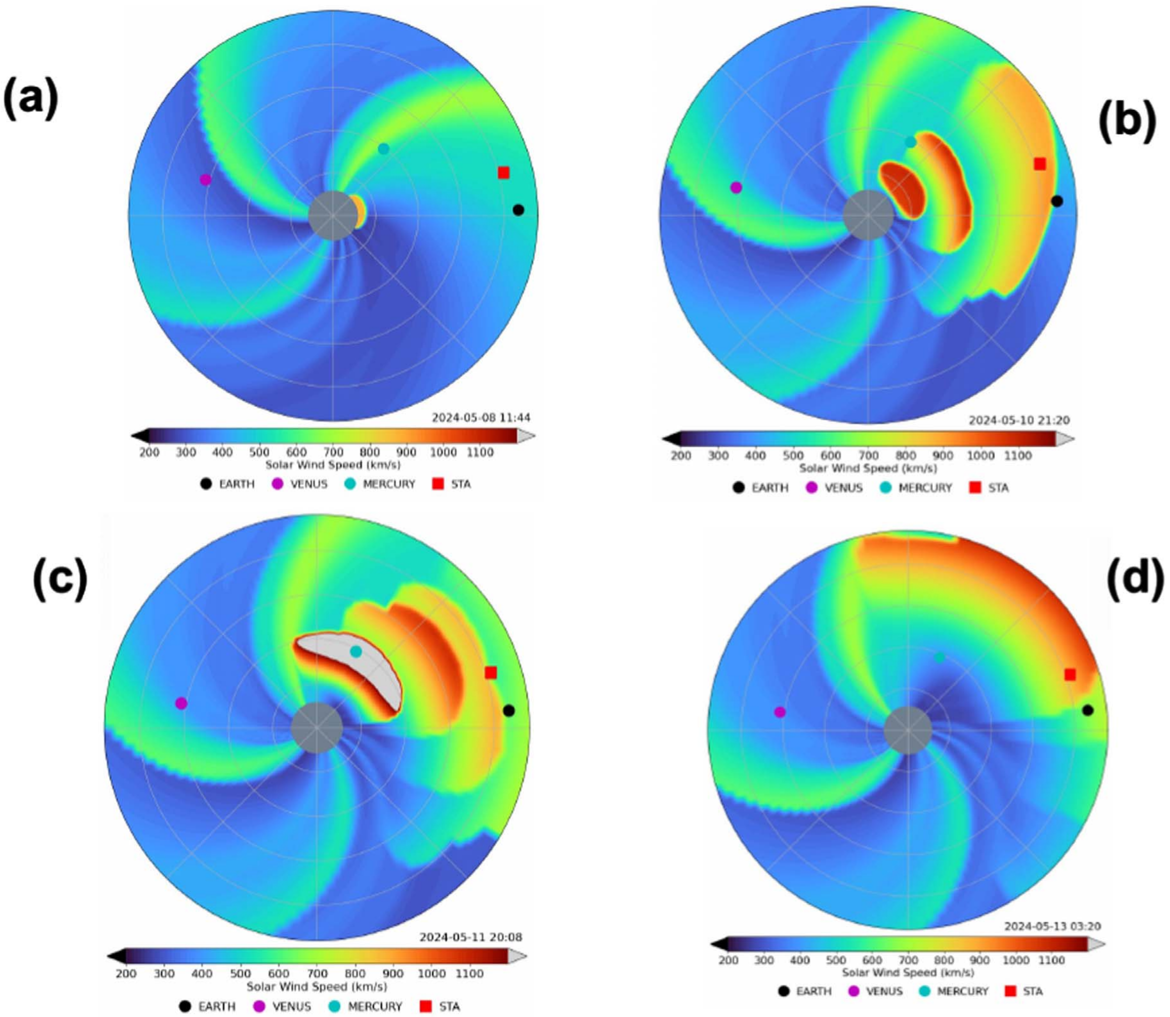

Figure 5. Snapshots from the STAR simulations. The solar wind velocity is shown in color. Different CMEs can be seen. The positions of Mercury, Venus, Earth, and the STEREO-A spacecraft are also shown. The UTC corresponding to each snapshot is given in the figure.

The first front represents the merged structure of the initial three CMEs (CME-1, CME-2, and CME-3), which had already crossed Earth's location by that time. These first three CMEs interacted with each other, causing their shocks to merge into a single front before reaching 1 au. This merging is also evident in the in situ speed profile shown in the bottom panel of Figure 6. The second CME front, corresponding to CME-4, is also visible in Figures 6(a) and (b) and has also passed Earth's location. At the time of the snapshot, CME-5 is passing through this location, while CME-6 is still behind.

When comparing the simulation results with ACE spacecraft observations, we found that the merged structure of CME-1, CME-2, and CME-3 arrived approximately 0.97 hr later than the observed arrival time. Additionally, the apex speed of the CMEs is almost the same in both the ACE (blue line) and SWASTi (red line) plots. The speed of the subsequent CME

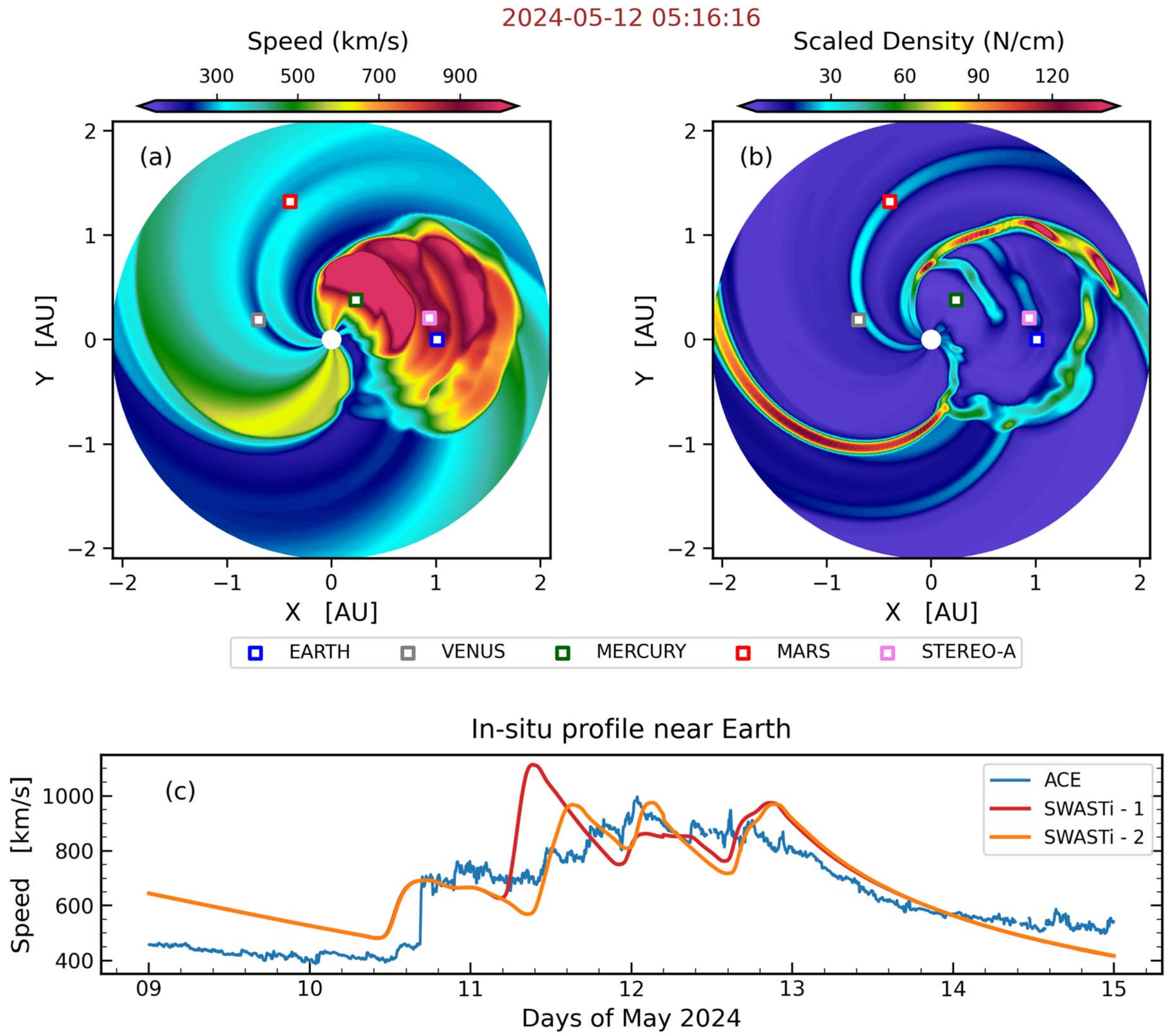

Figure 6. The figure demonstrates the simulation results from the SWASTi framework. Panels (a) and (b) show a time snapshot, at 2024-05-12T05:16, of the speed and scaled density in the equatorial plane, respectively. Panel (c) shows the in situ speed profile near Earth, where the blue line represents the ACE observational data and the red and orange lines correspond to the default (1) and tuned (2) SWASTi results, respectively.

(CME-4) front also shows a similar value in both in situ plots. However, there is a significant difference of approximately +11.2 hr in the simulated arrival time of CME-4 compared to the DONKI arrival time (see Figure 6(c)). It is important to note that the uncertainty regarding the initial density of the CME can significantly affect its arrival time. To demonstrate this, we conducted an additional simulation by reducing the density of CME-4 to $0.5 \times 10^{-18}\,\mathrm{kg\,m^{-3}}$.

The in situ plot of this additional SWASTi simulation (SWASTi-tuned) is represented by the orange line in Figure 6(c). A time difference of about 5.9 hr can be observed between the shock arrival times of the default and tuned versions of CME-4. Additionally, there is a difference of roughly $150\,\mathrm{km\,s^{-1}}$ in the apex speeds of CME-4. Interestingly, the change in the initial density of CME-4 not only affects the arrival properties of CME-4 itself but also impacts those of CME-5 and CME-6. This showcases the importance of estimating the initial density of CMEs to forecast their arrival times and properties accurately. This point is further highlighted by the fact that the overall RMSE of the default (SWASTi-1) run (from 2024 May 9 to 15) is approximately $120\,\mathrm{km\,s^{-1}}$, while that of the tuned (SWASTi-2) run is about $100\,\mathrm{km\,s^{-1}}$, reflecting a difference of 16.67% in overall accuracy.

However, the SWASTi simulations generate unexpectedly high density within the corotating interaction regions (CIR) at 1 au. The primary cause could be the greater-than-observed speed contrast between the fast and slow solar wind streams of that CIR in our simulation. This enhanced gradient artificially amplifies compression and makes the density values significantly higher than those recorded by WIND on May 16, where the relative speed contrast around CIR was much lower. While other regions and interaction structures within the same CR are well represented, this particular CIR density does not reflect the observed distribution as accurately, which highlights the need for refining the model to ensure more accurate density profiles.

As mentioned earlier, we have used the DBM, and flattening top geometry is used where each element of CME front propagated independently and tracked in the heliosphere. Figure 7 shows the heliospheric snapshot of all five CMEs when CME-1 reached Earth. Note that individual CMEs propagated based on the drag model and CME–CME interaction are not accounted for here. The DBM shows that

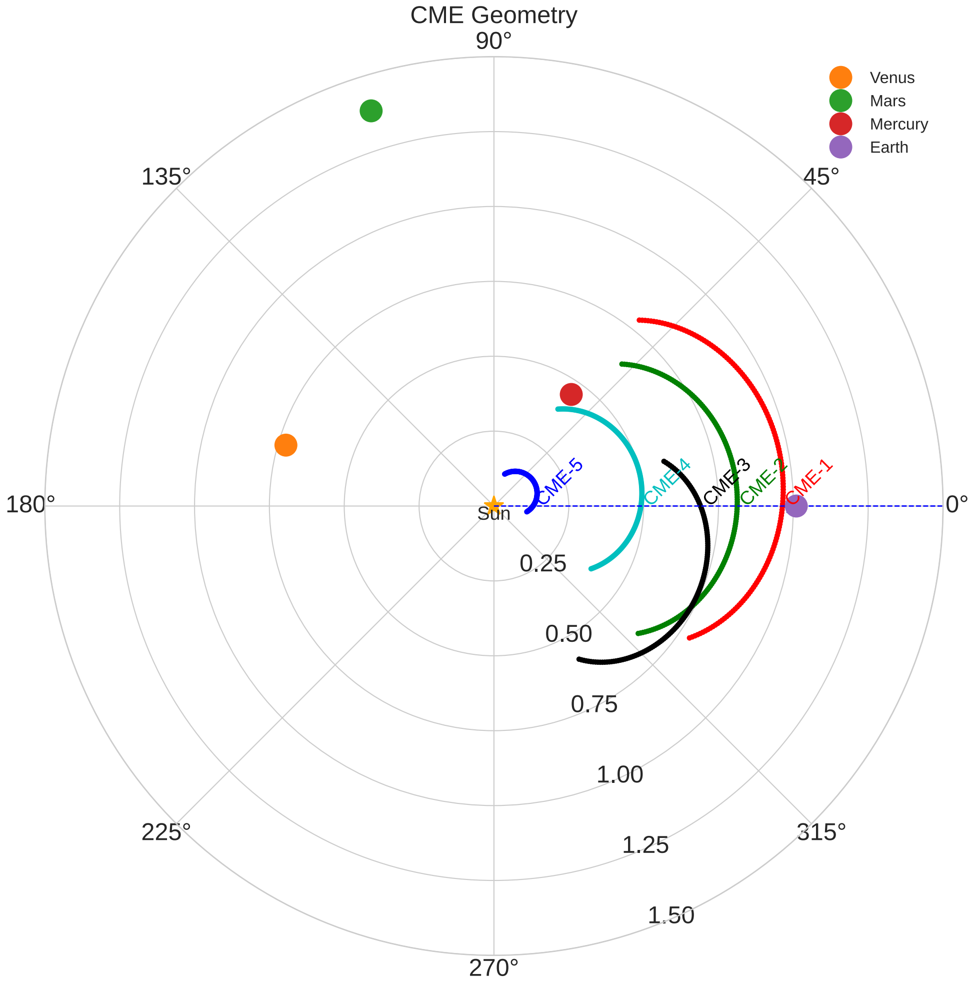

Figure 7. The CME fronts modeled based on the DBM model are shown for all five CMEs; the snapshot is at the time of arrival of CME-1 at Earth. Note that CME–CME interaction is not accounted for in the CME propagation.

all five of these CMEs directly or obliquely intersected Earth. Figure 8 shows how the velocity of each CME evolved during their radial-outward propagation in the interplanetary space. All CMEs started with high initial velocity at $21.5R_s$, and naturally their propagation velocity decreases as they move radially outward into the heliosphere. In this figure, the distance–time path (dashed line) of the front apex of each CME is shown. The distance–time paths come very close to each other for most of the CMEs, and CMEs are extended objects, indicating possible interaction between them before they reach Earth. Based on the model, we can estimate each CME's arrival time and velocity. However, the arrival time and velocity are subject to change depending on the uncertainty in the initial parameters of CME and background solar wind conditions. In reality, each measurement has some uncertainty; sometimes it is known, and sometimes it is unknown. Hence, we tried to conduct a sensitivity analysis of two variables: background solar wind velocity ($V_{\rm sw}$) and drag parameters (γ). These parameters are varied assuming Gaussian distributions (Figure 9), and then, using these ensemble samples, the arrival time, arrival velocity of CME, and transit time of CME for each pair of values were estimated.

Figure 9 shows the distribution of $V_{\rm sw}$ and γ, as these parameters represent background conditions for CME propagation. The mean background solar wind velocity was considered to be 450 km s^{-1}, having $3\sigma = 50$ km s^{-1}, whereas the mean drag parameter (γ) was considered to be 2×10^{-8}, having $3\sigma = 0.5 \times 10^{-8}$. Figure 10 presents the distributions of CME arrival velocity, arrival time at Earth, and transit time from the Sun to Earth for each CME listed in Table 1, obtained using the ensemble of inputs. The broad distribution of CME arrival velocity, arrival time, and transit time highlights the significant influence of the background solar wind speed and the drag parameter on the accuracy of forecasting CME arrivals at Earth (C. Kay et al. 2023; P. Mayank et al. 2023). The range of arrival velocities within the ensemble spans approximately $\sigma \sim 50$ km s^{-1} around the mean value, and the arrival times vary by approximately 3 hr σ, whereas the minimum to maximum values of arrival velocity span about ±100 km s^{-1}, and the arrival time spans about ±6 hr from the respective mean values. This variability underscores the complexities involved in predicting CME behavior and the need for precise modeling of the solar wind and drag effects to improve forecast accuracy.

Table 2 gives a summary of simulated CME arrival times and speeds, using STAR, the SWASTi code, and the DBM, along with the observed CME shock arrival times. For the STAR simulations, the results using the GONG-ADAPT maps are given. It can be seen that in the actual case also the first three CMEs arrived simultaneously, which was reproduced by

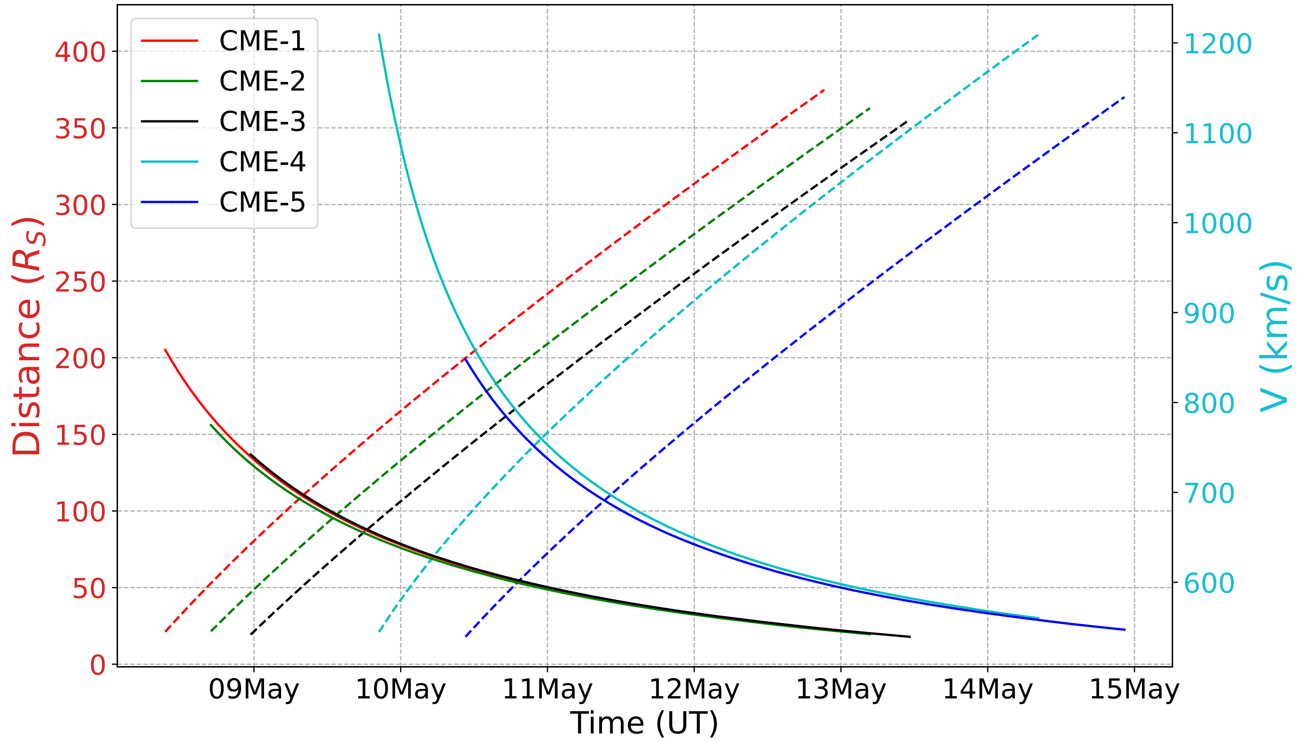

Figure 8. The DBM modeled CME's temporal evolution of velocity (solid lines) and radial distance (dashed lines) of the CME from the Sun. The colors indicate the modeled CME, and the dashed line indicates radial distance.

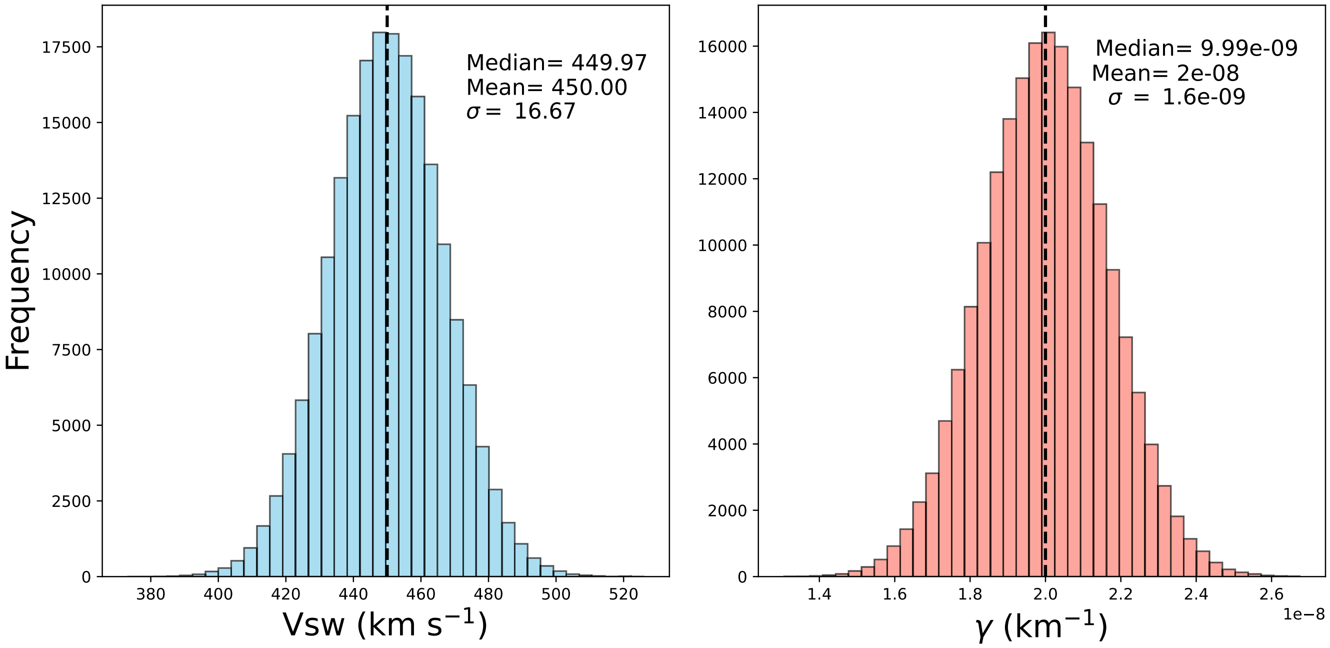

Figure 9. The Gaussian histogram of background solar wind velocity and drag parameter for the generated input parameter ensemble for the DBM model. For solar wind speed the mean is assumed to be 450 km s^{-1} and $3\sigma = 50$, whereas for γ the mean is assumed to be 2×10^{-8} and $3\sigma = 0.5 \times 10^{-8}$.

STAR and SWASTi. For CME-4 and CME-5, the difference between the arrival times is less than 2 hr as modeled by STAR. The shock related to CME-6 is not observed near Earth. The STAR simulations also show that the CME shock front did not directly hit Earth, whereas the DBM shows different arrival times of all these CMEs, with CME-1 reaching Earth almost 1 hr earlier than the observed shock arrival time. The DBM run for CME-2 and CME-3 shows arrival around 9 and 17 hr later than observed, respectively. For CME-4 and CME-5, the difference between the arrival times is around 3–8 hr. This indicates that STAR and SWASTi very closely predicted the arrival times of CMEs as compared to the DBM. Note that STAR and SWASTi account for the CME–CME interaction, whereas the DBM does not account for this. However, the arrival of CME-1 is very well predicted by all the studied models.

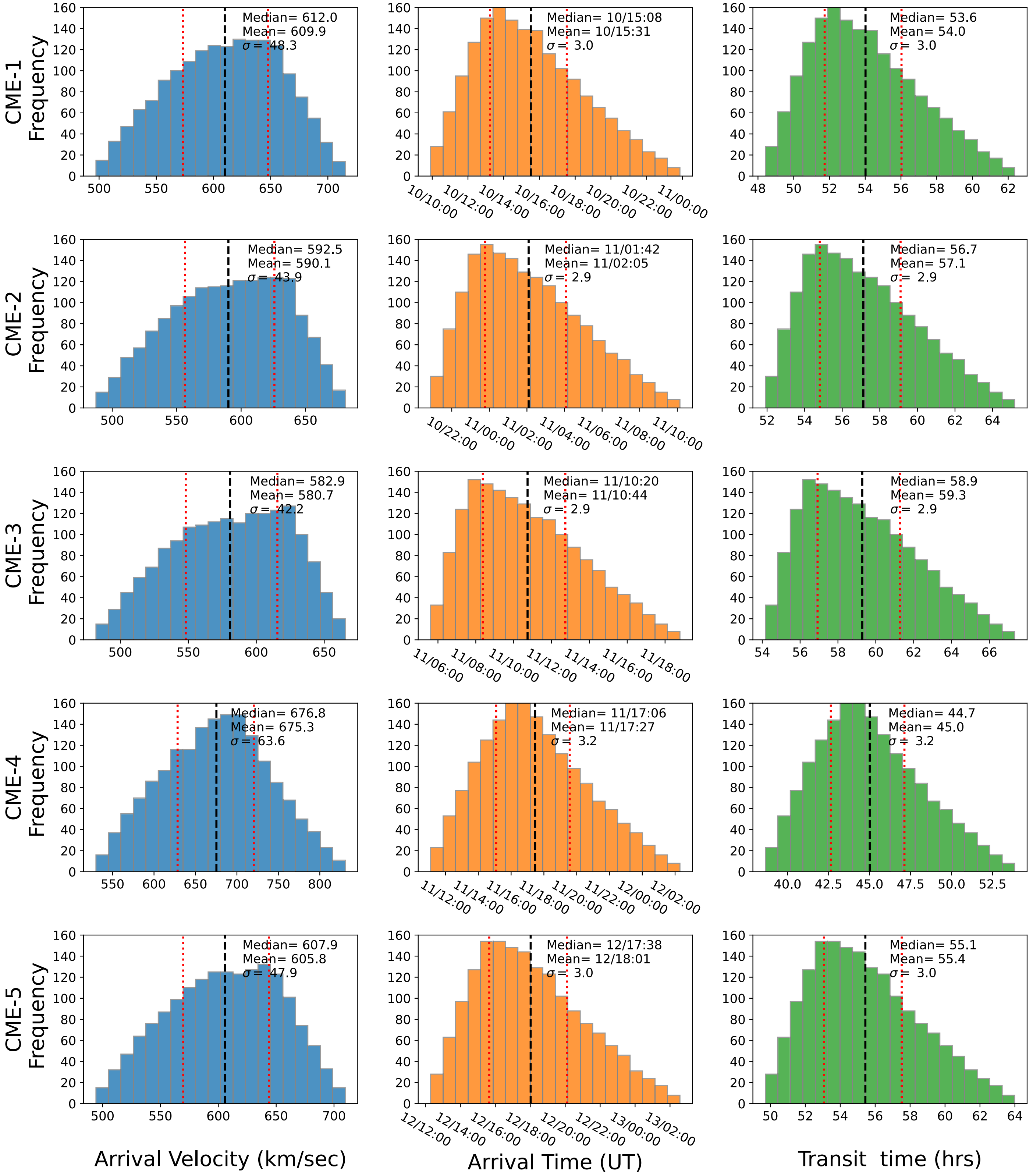

Figure 10. The histogram of the ensemble for each CME is shown for arrival velocity (blue), arrival time (orange), and transit time (green). Each row presents the parameters of the labeled CME. The frequency indicates the number of events falling in that particular bin of the distribution. The dashed vertical black line marks the mean value of the distribution, and the red vertical dotted lines from left to right mark the lower quartile (LQ) and upper quartile (UQ), respectively. CME labels at the left side indicate the CMEs listed in Table 1.

Table 2
Summary of Simulated CME Arrival Times and Speeds (km s^{-1}) at Earth

CME ID	DONKI Arrival Time	Arrival:STAR	Speed:STAR	Arrival:DBM	Speed:DBM	Arrival:SWASTi	Speed:SWASTi
CME-1	2024-05-10T16:36	−5.38	616	+1.08 ± 3.0 hr	609.9 ± 48.3	−0.97 hr	693
CME-2	2024-05-10T16:36	−5.38	616	−9.48 ± 2.9 hr	590.1 ± 43.9	−0.97 hr	693
CME-3	2024-05-10T16:36	−5.38	616	−17.73 ± 2.9 hr	580.7 ± 42.2	−0.97 hr	693
CME-4	2024-05-11T20:30	−1.53	745	+3.40 ± 3.2 hr	675.3 ± 63.6	+5.30 hr	968
CME-5	2024-05-12T08:55	−0.43	824	−8.72 ± 3.0 hr	605.8 ± 47.9	+5.85 hr	975

Note. For the STAR simulations, the results using the GONG-ADAPT map are given. For the DBM simulations, the mean speed and arrival times are given. The CME arrival time and speed corresponding to the SWASTi-2 simulation are also shown. The actual CME shock arrival times are taken from https://kauai.ccmc.gsfc.nasa.gov/CMEscoreboard/. The difference is taken from the observations with the model; hence, whenever the model-simulated arrivals are late, they are negative.

5. Discussion and Conclusions

The HUXt code has been developed in such a way that the boundary conditions can be accepted from a wide range of coronal models, including PFSS-based models such as WSA (C. N. Arge & V. J. Pizzo 2000) and MHD models such as Magnetohydrodynamic Algorithm outside a Sphere (MAS; P. Riley et al. 2001) and conditions derived from tomography such as CORTOM (K. A. Bunting & H. Morgan 2022). However, in most of the previous works (M. Owens et al. 2020) HUXt has been initiated with output from the MAS model. For example, M. Owens et al. (2020) performed the HUXt analysis with steady-state HelioMAS solutions as input for a period of 578 CRs. Based on several cases, they showed that the estimated CME transit times agreed to within 4 hr. In another recent study, the output from the Burger Radial Variational Data Assimilation (BRaVDA) scheme is used to define the solar wind speed structure at the inner boundary of HUXt (L. A. James et al. 2023). L. Barnard et al. (2023) used a sequential importance resampling (SIR) data assimilation scheme with the HUXt solar wind model and performed a set of theoretical experiments to show that SIR-HUXt can reduce the uncertainty on the CME arrival time and speed estimates, dropping by up to 69% and 63%, respectively, for an observer at the L5 Lagrange point. However, in this work no case studies of real CMEs in structured solar wind are shown.

In the present STAR framework, the inner boundary conditions for the HUXt module are provided from the semiempirical WSA relation obtained from PFSSPY making use of GONG maps, and CMEs are introduced via the cone CME parameterization to the model inner boundary. These simulations show that for this extreme space weather event the WSA+HUXt+cone CME–based simple simulations could predict the arrival times within a difference of ∼8 hr (CME-1–CME-3) or less (in the case of CME-4 and CME-5), which is comparable to the predictions of complex, computationally expensive MHD codes.

Simulations using the cone model in the SWASTi framework revealed that the merged shock front of CME-1, CME-2, and CME-3 arrived 0.97 hr later than observed by ACE, while CME-4's simulated arrival was delayed by 11.2 hr compared to DONKI predictions. Adjusting CME-4's initial density in a secondary simulation improved arrival time accuracy by 5.9 hr and reduced speed discrepancies, highlighting the critical role of accurate density estimation in forecasting CME properties.

Further, we compared these simulations by the STAR and SWASTi models with the DBM model outputs: arrival time and ICME velocity at Earth. It is observed that all models predicted the arrival time of the CMEs reasonably well. We also carried out the ensemble study for the DBM for varying background solar wind conditions and drag parameters. It has been observed that the arrival time and velocity of CME are sensitive to these background conditions, which are generally unknown, as also shown by other model simulations (e.g., M. Dumbović et al. 2018; P. Mayank et al. 2023). Even though we have not considered the uncertainty in the CME parameters, which definitely will affect arrival predictions, the DBM is still reasonably accurate in forecasting CME arrival time and velocity. The models for predicting the arrival of space weather events are generally able to get the CME shock arrival times to within ±10 hr, but with standard deviations often exceeding 20 hr (P. Riley et al. 2018).

The case study of a recent extreme space weather event provided a unique opportunity to evaluate the performance of the models for ICME arrival. For this event, the predictive simulations expected the arrival of ICME on late May 10 or Early May 11; however, the event arrived earlier compared to the predicted arrival times of several models,[6] including the present STAR, SWASTi, and DBM models. This implies that there is still improvement needed in models to match the observations, and future work will strive to improve the forecast of the arrival time of such extreme space weather events.

Acknowledgments

The work is supported by the Indian Space Research Organization. P.M. gratefully acknowledges the support provided by the Prime Minister's Research Fellowship. I.V. acknowledges the financial assistance provided by ISRO through a research fellowship. This work utilizes data produced collaboratively between the Air Force Research Laboratory (AFRL) and the National Solar Observatory (NSO). The ADAPT model development is supported by AFRL. The input data utilized by ADAPT are obtained by NSO/NISP (NSO Integrated Synoptic Program). The GONG-synoptic maps are taken from https://gong.nso.edu/data/magmap/. NSO is operated by the Association of Universities for Research in Astronomy (AURA), Inc., under a cooperative agreement with the National Science Foundation (NSF). The solar wind data are taken from the OMNIweb database (https://omniweb.gsfc.nasa.gov/). We thank the OMNIweb team for the data. This research made use of Astropy[7] (Astropy Collaboration et al.

---

[6] https://kauai.ccmc.gsfc.nasa.gov/CMEscoreboard/

[7] http://www.astropy.org

2013, 2018, 2022), a community-developed core Python package for Astronomy, version 4.0.0 of SunPy (S. Mumford et al. 2020; The SunPy Community et al. 2020), and the PFSSPY open-source software packages (D. Stansby et al. 2023). The HUXt code downloaded from GitHub[8] and Zenodo (M. Owens & L. Barnard 2024a) and the Advanced DBM model codes available on Zenodo are used in this work (R. Mugatwala & B. Vaidya 2021). We express our sincere thanks to the developers for providing these codes in open source. The frozen code of STAR is available on Zenodo (S. Thampi et al. 2025).

ORCID iDs

Smitha V. Thampi https://orcid.org/0000-0002-0116-829X
Ankush Bhaskar https://orcid.org/0000-0003-4281-1744
Prateek Mayank https://orcid.org/0000-0001-8265-6254
Bhargav Vaidya https://orcid.org/0000-0001-5424-0059
Indu Venugopal https://orcid.org/0009-0006-5587-1868

References

Arge, C. N., & Pizzo, V. J. 2000, JGR, 105, 10465
Astropy Collaboration, Price-Whelan, A. M., Lim, P. L., et al. 2022, ApJ, 935, 167
Astropy Collaboration, Price-Whelan, A. M., Sipőcz, B. M., et al. 2018, AJ, 156, 123
Astropy Collaboration, Robitaille, T. P., Tollerud, E. J., et al. 2013, A&A, 558, A33
Barnard, L., & Owens, M. 2022, FrP, 10, 1005621
Barnard, L., Owens, M., Scott, C., Lang, M., & Lockwood, M. 2023, SpWea, 21, e2023SW003487
Bothmer, V., & Schwenn, R. 1997, AnGeo, 16, 1
Bunting, K. A., & Morgan, H. 2022, JSWSC, 12, 30
Cargill, P. J. 2004, SoPh, 221, 135
Cargill, P. J., Chen, J., Spicer, D. S., & Zalesak, S. T. 1996, JGR, 101, 4855
Dumbović, M., Čalogović, J., Martinić, K., et al. 2021, FrASS, 8, 58
Dumbović, M., Čalogović, J., Vršnak, B., et al. 2018, ApJ, 854, 180
Hayakawa, H., Ebihara, Y., Willis, D. M., et al. 2019, SpWea, 17, 1553
Hayakawa, H., Nevanlinna, H., Blake, S. P., et al. 2022, ApJ, 928, 32
Hickmann, K. S., Godinez, H. C., Henney, C. J., & Arge, C. N. 2015, SoPh, 290, 1105
James, L. A., Scott, C. J., Barnard, L. A., et al. 2023, SpWea, 21, e2022SW003289
Kay, C., Nieves-Chinchilla, T., Hofmeister, S. J., Palmerio, E., & Ledvina, V. E. 2023, SpWea, 21, e2023SW003647
Lugaz, N., Manchester IV, W. B., & Gombosi, T. I. 2005, ApJ, 634, 651
Mayank, P., Vaidya, B., & Chakrabarty, D. 2022, ApJS, 262, 23
Mayank, P., Vaidya, B., Mishra, W., & Chakrabarty, D. 2023, ApJS, 270, 10
McGregor, S. L., Hughes, W. J., Arge, C. N., Owens, M. J., & Odstrcil, D. 2011, JGRA, 116, A03101
Mugatwala, R., & Vaidya, B. 2021, astronish16/DBM-Drag-Based-Model: First Release for DBM, v1, Zenodo, doi:10.5281/zenodo.5038647
Mumford, S., Freij, N., Christe, S., et al. 2020, JOSS, 5, 1832
Odstrcil, D., & Pizzo, V. J. 1999, JGR, 104, 28225
Owens, M., & Barnard, L. 2024a, University-of-Reading-Space-Science/HUXt: HUXT v4.2.0, Zenodo, doi:10.5281/zenodo.12772120
Owens, M., & Barnard, L. 2024b, University-of-Reading-Space-Science/HUXt: Minor Bug Fixes and Updated Environment, v.4.1.1, Zenodo, doi:10.5281/zenodo.10842659
Owens, M., Lang, M., Barnard, L., et al. 2020, SoPh, 295, 43
Pomoell, J., & Poedts, S. 2018, JSWSC, 8, A35
Riley, P., Linker, J. A., & Mikic, Z. 2001, JGR, 106, 15889
Riley, P., Mays, M. L., Andries, J., et al. 2018, SpWea, 16, 1245
Schrijver, C. J., Kauristie, K., Aylward, A. D., et al. 2015, AdSpR, 55, 2745
Schwenn, R., Dal Lago, A., Huttunen, E., & Gonzalez, W. D. 2005, AnGeo, 23, 10331059
Siscoe, G., Crooker, N., & Clauer, C. 2006, AdSpR, 38, 173
Stansby, D., Badman, S., Simon, T., Ancellin, M., & Barnes, W. 2023, dstansby/pfsspy: pfsspy v1.2.1, Zenodo, doi:10.5281/zenodo.2566461
Stansby, D., Yeates, A., & Badman, S. T. 2020, JOSS, 5, 2732
Thampi, S., Bhaskar, A., Mayank, P., Vaidya, B., & Venugopal, I. 2025, Solar Transient ARrival (STAR), version 1.0, Zenodo, doi:10.5281/zenodo.14615880
The SunPy Community, Barnes, W. T., Bobra, M. G., et al. 2020, ApJ, 890, 68
Tsurutani, B. T., Gonzalez, W., Lakhina, G., & Alex, S. 2003, JGRA, 108, 1268
Vršnak, B., Temmer, M., Žic, T., et al. 2014, ApJS, 213, 21
Vršnak, B., Žic, T., Vrbanec, D., et al. 2012, SoPh, 285, 295
Yamazaki, Y., Matzka, J., da Silva, M. V., et al. 2024, ESS Open Archive, doi:10.22541/essoar.171838396.68563140/v1

---

[8] https://github.com/University-of-Reading-Space-Science/HUXt/tree/v.4.1.1